JGR Oceans

RESEARCH ARTICLE
10.1029/2019JC015348

Key Points:
- Eddy generation in the North Pacific is highest in spring and lowest in fall except for the regions alongside the main Hawaiian Islands
- Mean anticyclone eddy intensity is significantly weaker than cyclone eddy intensity
- Regardless of eddy polarity, nonlinear (linear) eddies enhance larval retention (export) in island population of coral reef fish

Supporting Information:
- Supporting Information S1

Correspondence to:
D. Lindo-Atichati,
dlindo@whoi.edu

Citation:
Lindo-Atichati, D., Jia, Y., Wren, J. L. K., Antoniades, A., & Kobayashi, D. R. (2020). Eddies in the Hawaiian Archipelago Region: Formation, characterization, and potential implications on larval retention of reef fish. *Journal of Geophysical Research: Oceans*, *125*, e2019JC015348. https://doi.org/10.1029/2019JC015348

Received 7 JUN 2019
Accepted 14 APR 2020
Accepted article online 29 APR 2020

©2020. American Geophysical Union. All Rights Reserved.

Eddies in the Hawaiian Archipelago Region: Formation, Characterization, and Potential Implications on Larval Retention of Reef Fish

David Lindo-Atichati[1,2,3], Yanli Jia[4], Johanna L. K. Wren[5], Andreas Antoniades[2], and Donald R. Kobayashi[6]

[1]Department of Applied Ocean Physics and Engineering, Woods Hole Oceanographic Institution, Woods Hole, MA, USA, [2]Department of Earth and Planetary Sciences, American Museum of Natural History, New York, NY, USA, [3]Department of Engineering and Environmental Science,The City University of New York,Staten Island,NY,USA, [4]International Pacific Research Center, University of Hawai'i at Mänoa, Honolulu, HI, USA, [5]Joint Institute for Marine and Atmospheric Research, University of Hawai'i at Mänoa, Honolulu, HI, USA, [6]Ecosystem Sciences Division, Pacific Islands Fisheries Science Center, National Oceanographic and Atmospheric Administration, Honolulu, HI, USA

Abstract Here we present an assessment of eddy activity in a 3,500 × 2,000 km region of the North Pacific. Eddies were identified and tracked within a numerical simulation that used the Massachusetts Institute of Technology general circulation model and an eddy characterization algorithm. Spatially, eddy births were more frequent: (1) nearshore (cyclones) and offshore (anticyclones) on the windward side of the main Hawai'ian Islands; (2) in patches of cyclones and anticyclones that resembled the dipole structure of wind stress curl along the islands' leeward side; and (3) in zonal patches of eddies of both polarities west and north of the islands. Temporally, high eddy activities occurred in spring. There was a meridional distribution of eddy lifespans, which increased northward. Cyclones were more abundant, longer-lived, smaller, and more nonlinear. Reef fish spawning locations in Hawai'i coincide with the regions of high eddy activity, with nonlinear eddies responsible for high larval retention.

Plain Language Summary It has been well documented that rotating bodies of water—the so-called cyclonic and anticyclonic eddies—heavily influence biological productivity in the North Pacific. However, the dynamics of eddy formation and activity are not always clear, often lacking spatial resolution and statistical evaluation. Here we used a general circulation model and an eddy detection tool to provide a comprehensive description of ocean eddies in a 3,500 × 2,000 km region of the North Pacific. Our analysis revealed seasonality in eddy genesis for the whole region, with more eddies forming in spring. Eddy generation west of the Big Island of Hawai'i is consistent with the mechanism of formation by the strong dipole of wind stress curl. Notably, there are marked spatial patterns of eddy rotations, sizes, propagation speeds, and lifespans on both sides of the main Hawai'ian Islands. This work also sheds light on the linkages between eddy activity and retention of larval fish in the Hawai'ian Archipelago. Spawning sites of coral reef fish in Hawai'i coincide with most of the regions of high eddy activity. Interestingly, regardless of eddy polarity, nonlinear slow-propagating (fast swirling) eddies enhance larval retention while linear fast-propagating (slow-swirling) eddies enhance larval export and eventually larval dispersion.

1. Introduction

Mesoscale eddies are coherent rotating structures of water with horizontal length scales on the order of 10–100 km that are found all around the global ocean (Chelton et al., 2011). The knowledge of their spatial and temporal distribution, transport, and dynamics has been substantially improved, thanks to more than 20 years of sea level anomaly (SLA) satellite observations combined with the development of novel eddy tracking techniques (Ashkezari et al., 2016; Faghmous et al., 2015; Chelton et al., 2011; Mason et al., 2014). Leveraging these tracking algorithms, several studies have analyzed mesoscale eddies through their surface signature in satellite images (Hausmann & Czaja, 2012; Chelton et al., 2011; Wang et al., 2015; Gaube et al., 2015; Melnichenko et al., 2017), while others have combined these satellite measurements with Argo float temperature and salinity profiles to estimate their transport properties (Amores et al., 2017; Chaigneau et al., 2011; Pegliasco et al., 2015; Schütte et al., 2016). However, recent findings on rotationally coherent

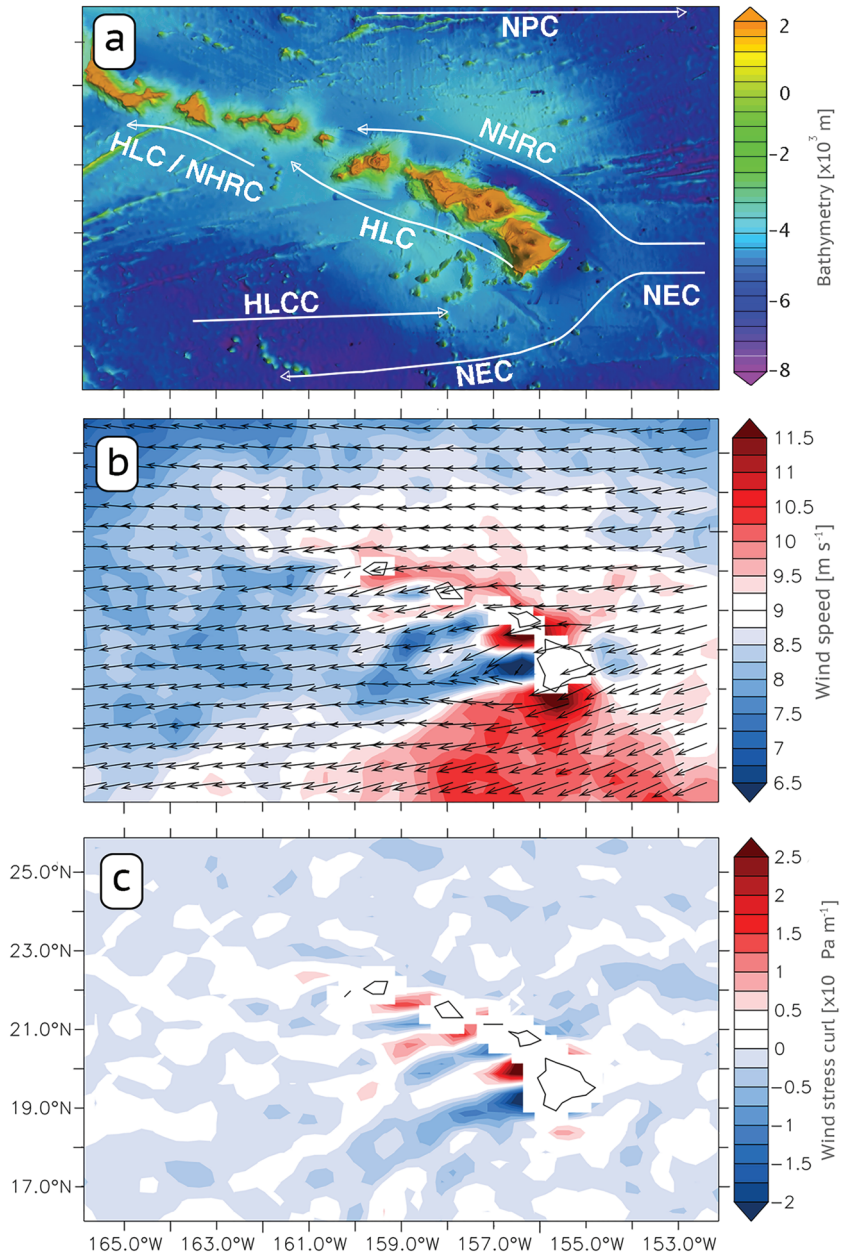

Figure 1. (a) Schematic map of the mean currents in Hawai'i (adapted from Lumpkin, 1998) overlaid on 1-min ocean bathymetry from ETOPO1 (Amante & Eakins, 2009). (b) ASCAT wind vectors and wind speed (m s^{-1}) averaged over 1–7 August 2009. (c) ASCAT wind stress curl (10^{-6} Pa m^{-1}) averaged over 1–7 August 2009.

Lagrangian vortices strongly suggest that coherent sea level anomalies do not necessarily correspond to trapped water masses, even in SLA contours that are closed (Abernathey & Haller, 2018).

Increased eddy activity is observed in the Hawai'ian Archipelago. Located in the North Pacific Ocean, the archipelago consists of a chain of tiny islands, atolls, shoals, and banks (the Northwestern Hawai'ian Islands) in the northwestern sector (162–178.5°W and 23–28.5°N) and the eight populated main Hawai'ian Islands at the southeastern extremity (155–162°W and 19–23°N) (Figure 1a). The Northwestern Hawai'ian Islands are located south of the eastward flowing North Pacific Current and the main Hawai'ian Islands are located on the northern edge of the westward flowing North Equatorial Current (NEC). Upon encountering the Big Island (the southernmost island of the archipelago), the NEC continues westward, passing the southern tip of the island. A narrow band of northward shear flow is observed along the east side of the ridge forming a boundary current named the North Hawai'ian Ridge Current (NHRC; Mysak & Magaard,

1983; White, 1983). This ridge current is highly variable and populated by energetic mesoscale eddies (see Qiu et al., 1997 and references therein for further description of this current). North of the NHRC we find the east flowing North Pacific Current (NPC) (Howell et al., 2012).

To the west of the main Hawai'ian Islands, oceanic circulation is vigorously affected by the obstacle that the islands represent to the prevailing northeast trade winds. Strong winds channel through gaps and flow around island flanks, and weak winds (or wind wake) form west of each island (or a cluster of islands), creating strong wind shear downwind of the islands (Figure 1b). The effect of this wind shear on the underlying ocean as represented by the wind stress curl is a series of dipoles, one pair downwind of each island, positive (negative) in the north (south) (Figure 1c). The resulting Ekman pumping generates upwelling in regions of positive wind stress curl and downwelling in regions of negative curl. These dipoles also have profound effects on ocean circulation to the west of the archipelago. The eastward flowing Hawai'ian Lee Counter Current (HLCC), characterized by Qiu et al. (1997), is driven by the strongest dipole west of the Big Island (Chavanne et al., 2002; Xie et al., 2001). Similarly, the Hawai'ian Lee Current (HLC), identified by Lumpkin (1998), is hypothesized to be part of the recirculation of HLCC in the form of a β plume (Jia et al., 2011). Furthermore, field surveys have shown that strong mesoscale eddies emerge west of the Big Island (Dickey et al., 2008; Lumpkin, 1998; Patzert, 1969). Patzert (1969) hypothesized that these eddies were induced by winds, with cyclonic eddies spun up in the upwelling region and anticyclonic eddies in the downwelling region. Numerical model experiments support this hypothesis (Calil et al., 2008; Jia et al., 2011; Kersale et al., 2011).

Farther west from the islands, away from the direct influence of the strong dipoles in the wind stress curl, there also exists substantial mesoscale variability. Kobashi and Kawamura (2002) suggested that baroclinic instability along the density front associated with HLCC is a principle generation mechanism for eddies in this region. Using model simulations, Yu et al. (2003) determined that there was considerable energy conversion from the mean flow to eddies by baroclinic (vertical flow shear) and barotropic (horizontal shear between NEC and HLCC) instabilities.

In contrast to what is known about mesoscale circulation features and eddy formation dynamics, little is known about the statistics of eddy births, amplitudes, scales, intensities, most likely pathways, lifetimes, propagation speeds, and nonlinearities in the region. Also, there is an incomplete understanding of how these eddy statistics vary between cyclonic and anticyclonic eddies. The main goal of the present work is to prescribe a purely Eulerian assessment of eddy activity in the Hawai'ian Archipelago. To this end, we conduct a simulation with the Massachusetts Institute of Technology general circulation model that resolves mesoscale eddies and also permits submesoscale eddy generation, apply an eddy detection algorithm to investigate eddy characteristics and their distributions, and finally discuss possible dynamic mechanisms and potential implications for dispersal of larval fish.

2. Model and Methods

We used an implementation of the Massachusetts Institute of Technology general circulation model (MITgcm; Marshall et al., 1997), which solves the incompressible Navier-Stokes equations discretized into finite volumes on a sphere. Subgrid-scale horizontal mixing was parameterized by Laplacian operators with constant coefficients of 50 $m^2\ s^{-1}$ for viscosity and 10 $m^2\ s^{-1}$ for tracer diffusion. Vertical mixing was specified with the k-profile parameterization of Large et al. (1994), with background coefficients of $10^{-4}\ m^2\ s^{-1}$ for viscosity and $10^{-5}\ m^2\ s^{-1}$ for diffusivity. The horizontal extent of our domain was set to 175°E–150°W and 15–35°N, a 35 × 20° region encompassing the Hawai'ian Archipelago. Ocean depth was defined by the ETOPO1 database (Amante & Eakins, 2009), with the boundaries of the continents defined by the 10-m bottom contour. The model grid had a constant horizontal resolution of 0.04° (~4 km), and 50 vertical layers with thickness that varied from 5 m at the surface to 510 m at the bottom. At the surface, our model was forced by wind stress and heat and fresh water fluxes. Wind stress was computed using the bulk formulae of Large and Pond (1981) from the Advanced Scatterometer (ASCAT) observed winds at a resolution of 0.25° (Bentamy & Croize-Fillon, 2012). Atmospheric variables from the European Centre for Medium-Range Weather Forecasts Interim Reanalysis (Dee et al., 2011) at a resolution of 1.0° were used for computing heat and fresh water fluxes based on the bulk formulae of Large and Pond (1982). Ocean temperature, salinity, and horizontal velocities from the global ocean prediction system based on the Hybrid Coordinate Ocean Model (HYCOM; Chassignet et al., 2009) were used to define the initial and lateral boundary conditions. Model simulation was run for the period of March 2009 to May 2014. Model variables, including sea surface

height, were saved as daily averages. We computed SLA by subtracting the mean sea surface height averaged over the integration period from the daily averages.

Our ocean circulation model then delivered SLA as inputs to the py-eddy-tracker code, an algorithm that makes possible the identification and tracking of ocean eddies and their associated properties (Mason et al., 2014). The algorithm of py-eddy-tracker SLA based is inspired by the largely accepted and widely used procedures described by Penven et al. (2005), Chelton et al. (2011), and Kurian et al. (2011). The code works with contours of SLA, and the details of the identification and tracking method we used are explained in pages 1,182–1,183 of Mason et al. (2014) and pages 3,332–3,334 of Mason et al. (2017). The limits of the tracking domain were set to a 33 × 18° area (176°E to 151°W, 16–34°N) for the period 1 May 2009 to 26 May 2014. Not any closed contour of SLA was used for eddy detection. Closed contours must meet a series of five criteria relating to its shape and interior characteristics:

(i) Pass a shape test with error ≤55%, where the error is defined as the ratio between the sum of area deviations of closed contours from its fitted circle and the area of that circle.
(ii) Contain a pixel count I that satisfies $I_{min} \leq \mathrm{I} \leq I_{max}$, where $I_{min} = 8$ pixels and $I_{max} = 1{,}000$ pixels.
(iii) Contain only pixels with SLA values above (below) the current SLA interval value for anticyclonic (cyclonic) eddies.
(iv) Contain no more than one local SLA maximum (minimum) for an anticyclone (cyclone). This constraint differs from Chelton et al. (2011), who permit multiple local maxima/minima.
(v) Have amplitudes (A) that satisfy $A_{min} \leq \mathrm{A} \leq A_{max}$, where $A_{min} = 1$ cm and $I_{max} = 150$ cm.

These five criteria, barring the shape test and local minima/maxima threshold, are identical to that of Chelton et al. (2011). Closed SLA contours were designated as eddies following these five criteria and were referred to as the effective perimeters of the eddies (P_e). Eddy properties, including position, date, A, swirl speed (U), effective radius (L_e), and speed-based radius (L_s) were saved at each time step. L_e was defined as the radius of a circle with the same area as the region enclosed by P_e. L_s was defined as the radius of the circle with the same area as the region within the closed contour of SLA with maximum average U around the SLA contour. Regarding the lower limits on eddy radii detectability, we followed the work on effective resolution in ocean models by Soufflet et al. (2016) to choose an effective resolution of 16 km (about four times the spatial resolution of the model). This means that smaller-scale motions are damped by the numerical viscosity. Regarding the lower limits on eddy lifetimes used in this analysis, we followed Chelton et al. (2011) and Mason et al. (2014) to choose a threshold of lifetimes of 4 days (about four times the temporal resolution of the model). Full descriptions of how the properties were estimated are located in Mason et al. (2014) and Chelton et al. (2011). These methods do not include cyclogeostrophic effects, which may be important factors in the amplitude versus velocity of small scales and in low-latitude regions of the ocean (Shakespeare, 2016). A comparison of the results of this study with the eddy characteristics deduced including the role of curvature and cyclogeostrophic adjustments is deferred to a future investigation.

Finally, surface geostrophic velocities from the ocean circulation model were used in Lagrangian model. The methodology followed in this study to model dispersal of larval fish is similar to the methodology presented by Lindo-Atichati et al. (2016) and refined in Lindo-Atichati et al. (2019). Here, MITgcm provided surface geostrophic currents to Ocean Parcels (Lange & van Sebille, 2017; Van Sebille et al., 2017; Lindo-Atichati et al., 2019). Lagrangian frameworks compute Lagrangian trajectories by solving the following equation:

$$X(t + \Delta t) = X(t) + \int_{t}^{t+\Delta t} v(x, \tau)\, d\tau + \Delta X_s(t) \tag{1}$$

where $X(t)$ is the location of a water parcel at the surface and $v(x, \tau)$ is the surface geostrophic velocity of the water parcel at that position obtained from the outputs of MITgcm. $\Delta X_s(t)$ is a variation in location due to stochastic noise, which is added to represent unresolved subgrid scales following a random walk model (Griffa, 1996). A fourth-order Runge-Kutta interpolation scheme is used every time step Δt.

Two water parcels deployed simultaneously at the same location and time often follow very different paths due to the chaotic nature of nonlinear advection and unresolved subgrid-scale processes in ocean models (LaCasce, 2008; Mariano et al., 2002). To take into consideration for these uncertainties, we released simultaneously 1,000 synthetic larval fish (Lynch et al., 2014) at the centroid of eight different eddies: four cyclonic and four anticyclonic. Out of these eight eddies, six were linear and two were nonlinear eddies. We define

synthetic as virtual larval fish that are considered as passively drifting particles advected by surface currents. Eddy nonlinearity was computed as the quotient of the instantaneous eddy swirl speed divided by the instantaneous eddy propagation speed, U/C (Chelton et al., 2007). An eddy was designated nonlinear when U/C was greater than 1, and it was designated linear when U/C was less or equal than 1. Synthetic larval fish were tracked forward in time for 45 days, a typical pelagic larval duration for coral reef fish, using an integration time step of 5 min and horizontal diffusivity of 10 $m^2\ s^{-1}$ (Okubo, 1970).

3. Results and Discussion

3.1. Eddy Genesis and Propagation

An aggregate of 6,585 cyclonic eddies and 5,298 anticyclonic eddies were identified in the period 2009–2014 (Figure 2a).

To examine the spatial distribution of eddy generation, we summed the number of eddy births for each $0.5° \times 0.5°$ cell in the study region over the 5-year simulation period and then computed an annual average. As eddies propagate and their ages increase, they are not counted multiple times in the averaging on $0.5° \times 0.5°$ grid cells. The results are shown in Figure 2b for cyclonic eddies and Figure 2c for anticyclonic eddies. We observed sites of frequent eddy generation preferred by one or the other polarity leeward of the island, as well as regions with polarities located more than 300 km offshore west from the islands.

In the regions away from the vicinity of the islands, the most striking pattern in eddy generation was the zonally coherent banded structure, which was most notable in the distribution of anticyclonic eddy births (Figure 2c). In the southern part of the domain (south of 20°N), eddy generation resulted from barotropic and baroclinic flow instabilities related to the HLCC and NEC, as observed by Yu et al. (2003). In the northern part of the domain, examination of the model's flow field revealed occurrences of quasi-stationary and quasi-permanent jet-like structures. Zonal jets of similar characteristics have been noted in high-resolution ocean models (e.g., Nakano & Hasumi, 2005; Richards et al., 2006) and in observations (Maximenko et al., 2005, 2008). They are thought to be related to the dynamics of geostrophic turbulence on a β plane (Rhines, 1975) and are usually unstable.

We examine a region in which flows and presumable eddy generation are impacted by the main Hawai‘ian Islands (Figure 3). The leeward region is delimited by v1 (165°W, 23°N), v2 (162°W, 23°N), v3 (155°W, 19.5°N), and v4 (155°W, 17.5°N). The windward region is delimited by v2 (162°W, 23°N), v3 (155°W, 19.5°N), v5 (152°W, 19.5°N), and v6 (162°W, 25°).

In the islands' lee (black quadrilateral of Figure 3), local maxima of both eddy polarities occurred side by side. Dong et al. (2009) obtained a similar pattern in a regional model simulation. The pattern we found closely resembled the dipole structures in the curl of wind stress in this region (Figure 1c). Cyclonic and anticyclonic eddy generation determined from the SLA eddy tracking algorithm as the starting position and time of an identified closed SLA contour is visually similar to wind stress curl patterns and is not inconsistent with proposed wind stress curl eddy generation. This is consistent with findings of Jia et al. (2011), who discuss eddy generation mechanisms in detail. Here we also observed high eddy generation rates west of the smaller islands corresponding to the weaker dipoles. There has been observational evidence for eddy generation in this region. An anticyclonic eddy west of O‘ahu was detected by high-frequency radar (Chavanne et al., 2010) and had an approximate lifespan of approximately 2 weeks. Also, a cyclonic eddy formed west of Läna‘i and lasted approximately 9 days (Dong et al., 2009). Being in the category of submesoscale, neither was evident in the altimeter data. Signal noise from high-frequency motions (e.g., incoherent internal tides), noise in the measurements, and also the fact that SLA data are usually an interpolated field estimated from a few satellite measurements are three primary issues that must be solved in the future to resolve submesoscale eddies with altimetry (Chavanne & Klein, 2010). As we will see in the next section, eddies formed west of the smaller islands were generally small in size and short-lived compared with those formed west of the Big Island.

Along the NHRC (purple quadrilateral of Figure 3), cyclones were more frequently generated nearshore adjacent to anticyclonic polarity offshore. This pattern of alternating polarities is consistent with field observations in the region by Price et al. (1994). In two of their four surveys, cyclonic-anticyclonic pairs along windward (northeast) O‘ahu were present.

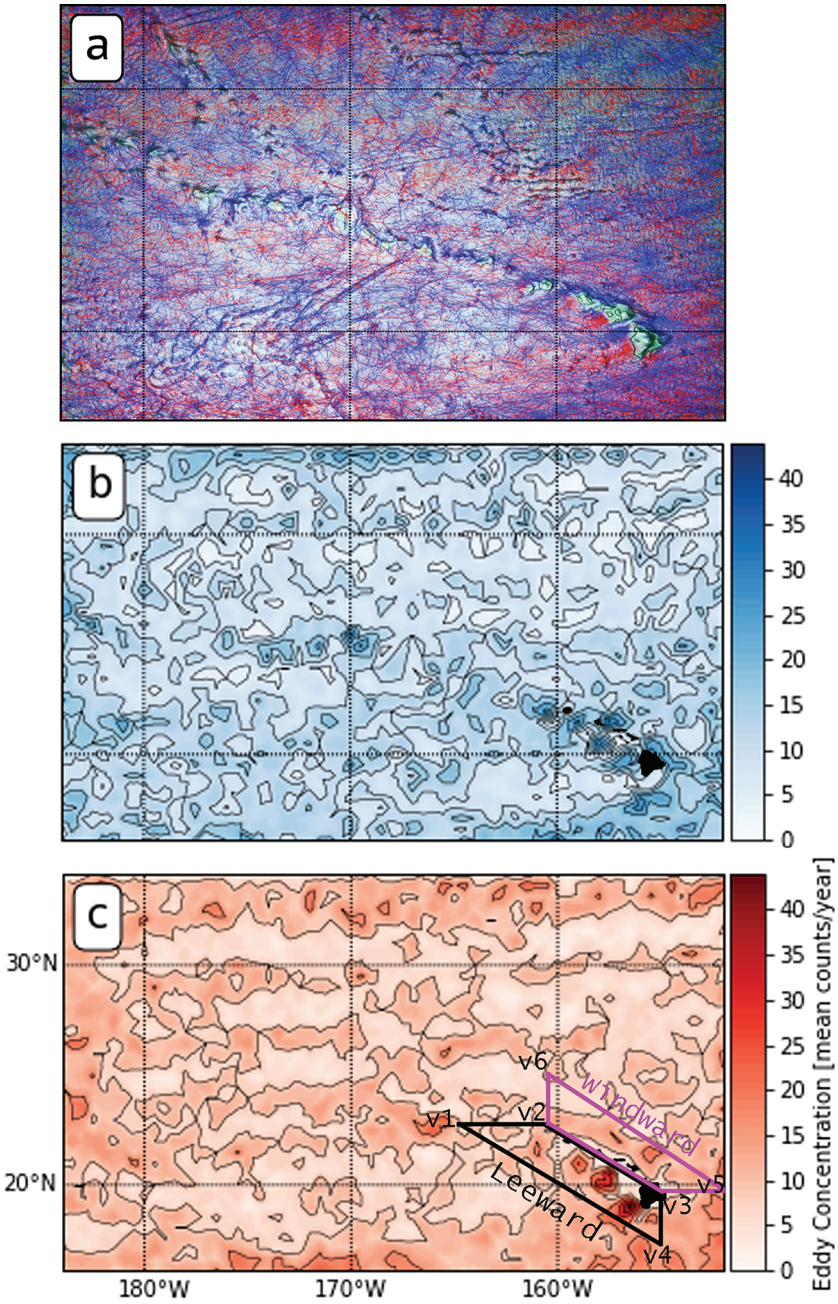

Figure 2. Eddy tracking in the Hawai'ian Archipelago. (a) Overlaid on 1-min ocean bathymetry, tracks of cyclonic (blue), and anticyclonic (red) eddies identified in a region of $68 \cdot 10^5$ km^2 from 2009 to 2014, Annual mean eddy birth concentrations (eddy counts on a $0.5° \times 0.5°$ grid) are presented for (b) cyclonic and (c) anticyclonic eddies over the study period of 5 years. Black and purple quadrilaterals of $2 \cdot 10^5$ km^2 each include the islands' lee region (leeward) and windward region (Windward). The coordinates of vertexes v1–v6, and enlarged figures of eddy birth in the quadrilaterals are provided in Figure 3.

To examine the temporal variability of eddy generation in the region, we summed the number of eddy births for each month of the 5 years for the whole domain (Figures 2b and 2c) and for the two subregions leeward and windward of the islands (black and purple quadrilaterals in Figure 3). The time series for the whole domain (Figure 4a) shows that cyclonic eddies were generated more frequently than anticyclonic eddies, with 24% more cyclones than anticyclones for lifetimes longer than 1 week and radii greater than 10 km. A slight preference for cyclonic over anticyclonic eddies was also observed globally, with 6% more cyclones than anticyclones for lifetimes longer than 16 weeks and radii greater than 40 km (Chelton et al., 2011).

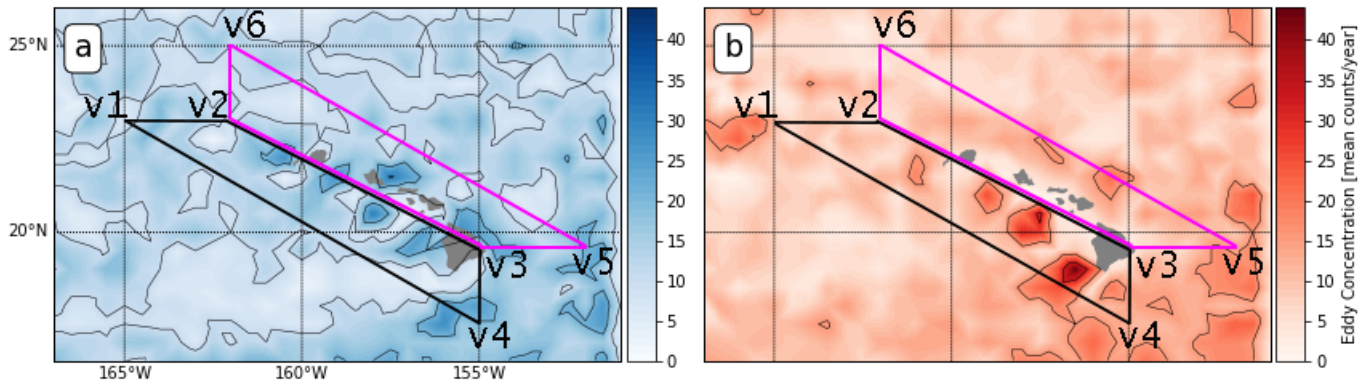

Figure 3. Annual mean eddy birth concentrations (mean eddy counts on a 0.5 × 0.5° grid per year) are shown for (a) cyclonic and (b) anticyclonic eddies over the 5-year study period. Black and purple quadrilaterals of $2 \cdot 10^5$ km^2 each include the islands' leeward and windward regions, respectively.

In our study, a slight preference for cyclonic over anticyclonic eddies was also present for lifetimes longer than 16 weeks and radii greater than 40 km, with 2% more cyclones than anticyclones. There was a definite seasonal cycle with a higher rate of eddy births in spring than in fall. Such a seasonal cycle of eddy variability has been shown by Kobashi and Kawamura (2002) and Liu et al. (2012) for the southern part of our domain (NEC and HLCC region) and by Chen and Qiu (2010) for the northern part of the domain. Large growth rate of baroclinic instability during winter from strong vertical velocity shear and weak upper ocean stratification leads to a maximum in eddy energy in spring. This seasonal variability, however, was not apparent in the two subregions (Figure 4b), reflecting the very different regional circulation characteristics affected by the islands' presence in the background subtropical gyre circulation. While the seasonal variability was clear in the whole analysis region for eddies with any radius, in the Leeward and Windward region it was less apparent for eddies with radius less than 25 km, and there was not seasonal variability for eddies with radius greater than 25 km (Figures S4 and S5). Additionally, while more cyclonic eddies were also generated in the leeward subregion, eddy births of both polarities were comparable in the windward subregion.

Consistent with predictions of westward eddy propagation at Rossby wave like speeds on a β plane, all eddies propagated westward (Figure 5a). Their meridional directions varied regionally. Eddies in the northern part of the domain had a weak but discernible southward component. Eddy tracks indicate that cyclonic eddies that formed west of the Big Island moved northwestward while anticyclonic eddies initially traveled southwestward then primarily westward. Eddies of both polarities generated in the NHRC followed the direction of the current, although some of the cyclonic eddies crossed the ridge between Kaua'i and O'ahu toward the southwest. Eddies formed west of the smaller islands generally did not move far from their birth sites during their relatively short lifetimes, ranging from 5 to 15 weeks for cyclones and from 1 to 5 weeks for anticyclones. In particular, the group of four smaller islands including Maui has short tracks ranging from 30 to

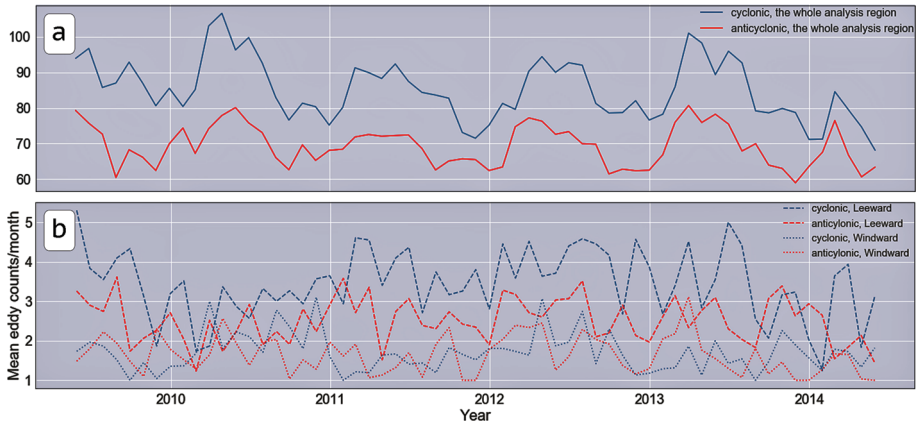

Figure 4. (a) Monthly counts of cyclonic and anticyclonic eddies for the whole of the analysis region and (b) for the Leeward and Windward regions over the 5-year study period.

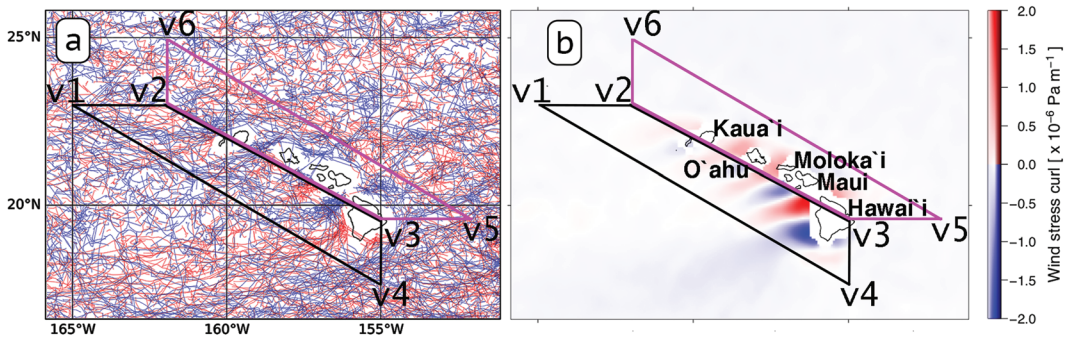

Figure 5. (a) Tracks of cyclonic (blue) and anticyclonic (red) submesoscale and mesoscale eddies identified in the islands' leeward and windward regions and (b) the ASCAT wind stress curl (10^{-6} Pa m^{-1}) averaged over May 2009 to May 2014.

250 km and moderately short lives ranging from 1 to 15 weeks. This means that these eddies may interact with the cyclonic eddies that propagate from one formation region (such as the Big Island) to the lee of the smaller islands but the former dominate (being larger, stronger, and long-lived). Interestingly, the majority of eddies that cross the two passages around Kaua'i are cyclones and propagate southwestward. The major generation sites of cyclonic and anticyclonic eddies match very well with the positive and negative poles of the wind stress curl in the immediate lee of the islands (Figure 5b). This match is consistent visually as a pattern of the wind forcing mechanism.

Overall, the model's representation of eddy generation and propagation was in good agreement with existing observations (e.g., Chavanne et al., 2010; Dickey et al., 2008; Lumpkin, 1998; Price et al., 1994; Zhang et al., 2019) and consistent with present understanding of eddy generation mechanisms in the study region (e.g., Calil et al., 2008; Castillo-Trujillo et al., 2019; Jia et al., 2011; Kersale et al., 2011; Powell, 2017; Yu et al., 2003).

3.2. Eddy Intensity and Age

The spatial variability of eddy properties were unfolded in maps of annual mean eddy amplitude, radius, intensity, and age. Eddy intensity was computed as the ratio between the amplitude and the effective radius of an eddy (A/L_e) (Frenger et al., 2015), and eddy age was defined as the lifetime or period of time that encompasses birth, growth, mature, decay, and death phases of the eddy. Only eddies of ages of 30 weeks or less are considered in the analysis since they represent 99.5% of the eddies formed in our region and period of study. The tracking method used here has an identification threshold in which the effective perimeter of the eddy does not contain more than one local SLA maximum (minimum) for an anticyclone (cyclone). That strict threshold prevents mismatching of connections from eddies at consecutive frames that would artificially increase eddy lifetimes, as shown in the comparisons with the Chelton et al. (2011) data made by Mason et al. (2014). The striking feature common to the maps in Figure 6 was the large-scale pool of maximum property means that was centered west of the Big Island. This feature was most imprinted in the fields of eddy amplitude and eddy intensity, where the neighboring amplitudes (0–5 cm) and intensities (0–0.1 cm km^{-1}) were evenly low (Figures 6a, 6b, 6e, and 6f). For anticyclones, this large-scale pool of large eddy amplitude, radius, and intensity was more elongated than for cyclones. For example, the pool of large intensities for anticyclones was 530 km more elongated than for cyclones and reached 165°W. Overall, the geographical distribution of the effective radius of an eddy was characterized as an essentially gradual decrease from about 70 km at 20°N to about 55 km at 30°N, which represents a decrease of approximately 20% in the effective radius from 20°N to 30°N. That pattern in concert with the observed global monotonic decrease of mean eddy scales from about 120 km at 20°N to about 90 km at 30°N, which represents a decrease of approximately 25% in the effective radius from 20°N to 30°N (Figure 12, right panel, of Chelton et al., 2011). These scales are comparable to the Rossby radius of deformation, which decreases from about 65 km to about 40 km over the same latitude range (Chelton et al., 1998).

Eddy amplitudes were also high in the northwestern subregion (Figures 6a and 6b). For anticyclones, there were various small patches of high amplitudes along the NHRC. Anticyclones were generally larger than cyclones. Of remarkable note for anticyclones was the 200 km peak of eddy radii along the southern boundary of the HLCC front and the 150 km peak of eddy radii along the NHRC front (Figure 6d).

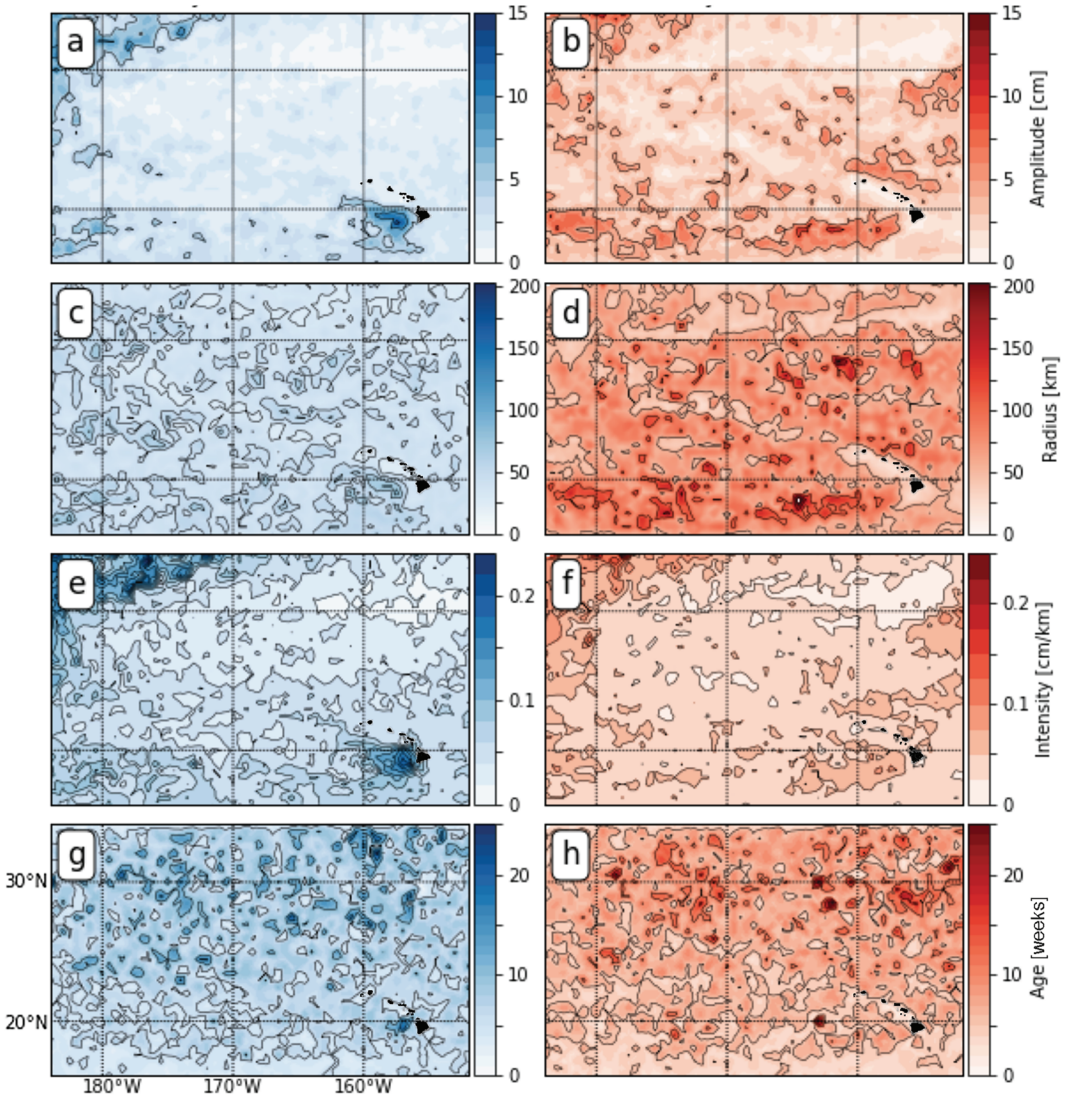

Figure 6. Contour plots of annual mean eddy amplitude (a and b), radius (c and d), intensity (e and f), and age (g and h) of eddies on a 0.5 × 0.5° grid. Cyclonic eddy properties are shown in blue, and anticyclonic eddy properties are shown in red.

The combination of eddy amplitude and radius into the eddy intensity calculation unambiguously revealed a number of regions of high eddy intensity (Figures 6e and 6f). For cyclones, these regions corresponded to the intersection of the HLCC and HLC, the HLC, and the northwestern subregion north of 30°N and west of 170°W. The latter was not an artifact of forcing issues at the domain boundaries. It has also been detected in modeling and observational works by Qiu and Chen (2010) and Cheng et al. (2014). For anticyclones, there was a wider area of high eddy intensity south of the HLCC from 156°W to 165°W, and in the northwestern subregion north of 30°N and west of 170°W. Interestingly, mean cyclone eddy intensity was significantly stronger than anticyclone eddy intensity. This is consistent with the mean cyclone and anticyclone eddy intensities reported by Gaube et al. (2015) for all midlatitudes eddies (15°–45°N) and for the Hawai'ian Ridge (15°–25°N, 180°–220°E). In their observational study, Gaube et al. (2015) showed that higher cyclone eddy intensities are due to cyclonic eddies having slightly greater amplitudes and smaller radius than anticylones in midlatitudes and in the the Hawai'ian Ridge (Figure 1 and Table 1 of Gaube et al., 2015). In our modeling work, centered geographically in the Hawai'ian Archipelago, higher cyclone eddy intensities are likely due to cyclonic eddies having smaller radius than anticylones. We can hypothesize that high cyclonic activity of strong intensity might be affecting water mass transport and eddy driven mixing along the HLC and the intersection of the HLCC and the HLC. However, testing the previous hypothesis is out of the scope of this

manuscript. The distributions of amplitude and intensities and the ratios of cyclonic to anti cyclonic eddies are presented in subsection 3.3.

In contrast to patterns in eddy intensity, maps of mean eddy age were similar for cyclones and anticyclones (Figures 6g and 6h). The age of eddies decreased 1 order of magnitude moving north to south, ranging from a mean age of 20 ± 5 weeks at 28°N to a mean age of 3 ± 2 weeks at 18°N. Figure 6 also showed that eddies formed west of the smaller islands were smaller, weaker, and shorter-lived than those formed west of the Big Island. This pattern is also consistent with observations of Gaube et al. (2015).

Many different methods have been used to identify coherent structures. These methods fall into two general categories: Eulerian and Lagrangian. Eulerian methods are based on instantaneous features of the velocity field, while Lagrangian methods are based on time-dependent trajectories of water parcels. Early Eulerian approaches used contours of the Okubo-Weiss parameter to identify the boundaries of eddies (Isern-Fontanet et al., 2003; Okubo, 1970; Weiss, 1991) and, more recently, closed contours of SLA (Chelton et al., 2011; Mason et al., 2014, 2017). The latter have been widely adopted by the community, likely due to its open source publication, and have been applied in this manuscript. These Eulerian approaches to eddy tracking may have the limitation that these features do not necessarily represent the same fluid (see Haller, 2015, and Peacock et al., 2015, for a discussion). Recently, Abernathey and Haller (2018) compiled these ideas and introduced a methodology to identify and track Rotationally Coherent Lagrangian Vortex (RCLV) based on a dynamic polar decomposition of the deformation gradient. Globally, RCLVs (Lagrangian) and SLA eddies (Eulerian) derived from satellite altimetry were found to propagate westward at similar speeds at each latitude, consistent with the Rossby wave dispersion relation. However, RCLVs were smaller and shorter-lived than SLA eddies identified from SLA (Chelton et al., 2011). Although we can assume that at global scales discrepancies on eddy radius and lifetime hold for our Chelton et al. (2011) derived method, we did not observe them when we released Lagrangian water parcels inside different types of eddies (see Figure 8). Analyzing global scales discrepancies on eddy radius and lifetime derived from applying Eulerian and Lagrangian methods to an ocean model is out of the scope of this work but will be a worthwhile endeav or to pursue.

3.3. Eddy Ratios and Nonlinearities

Distributions of eddies of lifetimes, radii, amplitudes, and nonlinearities are shown in Figure 7. The annual mean numbers of cyclonic and anticyclonic eddies with lifetimes between 1 and 35 weeks had similar distributions (Figure 7a). Remarkably, there were 10 times more eddies with a lifetime of 1 week compared to eddies with a lifetime of 5 weeks. That tenfold decrease in number of eddies is very similar to the one observed globally for lifetimes between 5 and 15 weeks (Figure 2, top left, of Chelton et al., 2011). For lifetimes greater than 12 weeks, the eddy count was mostly fewer than 10 eddies per year. We found no polarity dominance at lifetimes less than 25 weeks, yet cyclonic dominance was apparent for lifetimes between 25 and 65 weeks. Cyclonic (anticyclonic) polarity dominance was also observed globally for lifetimes shorter (longer) than 65 weeks (Figure 2, bottom left, of Chelton et al., 2011).

The annual mean numbers of cyclonic and anticyclonic eddies with radii between 13 and 100 km had comparable distributions (Figure 7c). In the range of radii from 30 to 60 km, there tended a greater number of eddies with radii less than 35 km. In fact, there were five times more eddies with a radius of 30 km compared to those with a radius of 60 km. For radii greater than 100 km, the eddy count was fewer than 10 per year. Eddies with radii smaller (larger) than 45 km were predominantly cyclonic (anticyclonic) (Figure 7d).

The annual mean numbers of cyclonic and anticyclonic eddies had resembling distributions for all amplitudes (Figure 7e). In the range of amplitudes from 1 to 5 cm, there tended a greater number of eddies with radii less than 50 km. In fact, there were 10 times more eddies with an amplitude of 1 cm compared to those with an amplitude of 5 cm. For amplitudes greater than 6 cm, the eddy count was fewer than 10 eddies per year. There was no clear polarity dominance in eddy amplitude (Figure 7f).

The annual mean numbers of linear ($U/C < 1$) cyclonic and anticyclonic eddies had similar distributions (Figure 7g). In the range of nonlinearities from 0.1 to 0.3, there tended a greater number of eddies with radii more than 50 km. There were 10 times more eddies with a nonlinearity of 0.1 compared to those with a nonlinearity of 0.3. The annual eddy count of nonlinear eddies ($U/C > 1$) was mostly fewer than 10 eddies per year. Three nonlinear anticyclonic eddies and nine nonlinear cyclonic eddies were depicted in Figure 7g, which illustrates a clear cyclonic dominance of nonlinear eddies. The presences of more nonlinear cyclonic

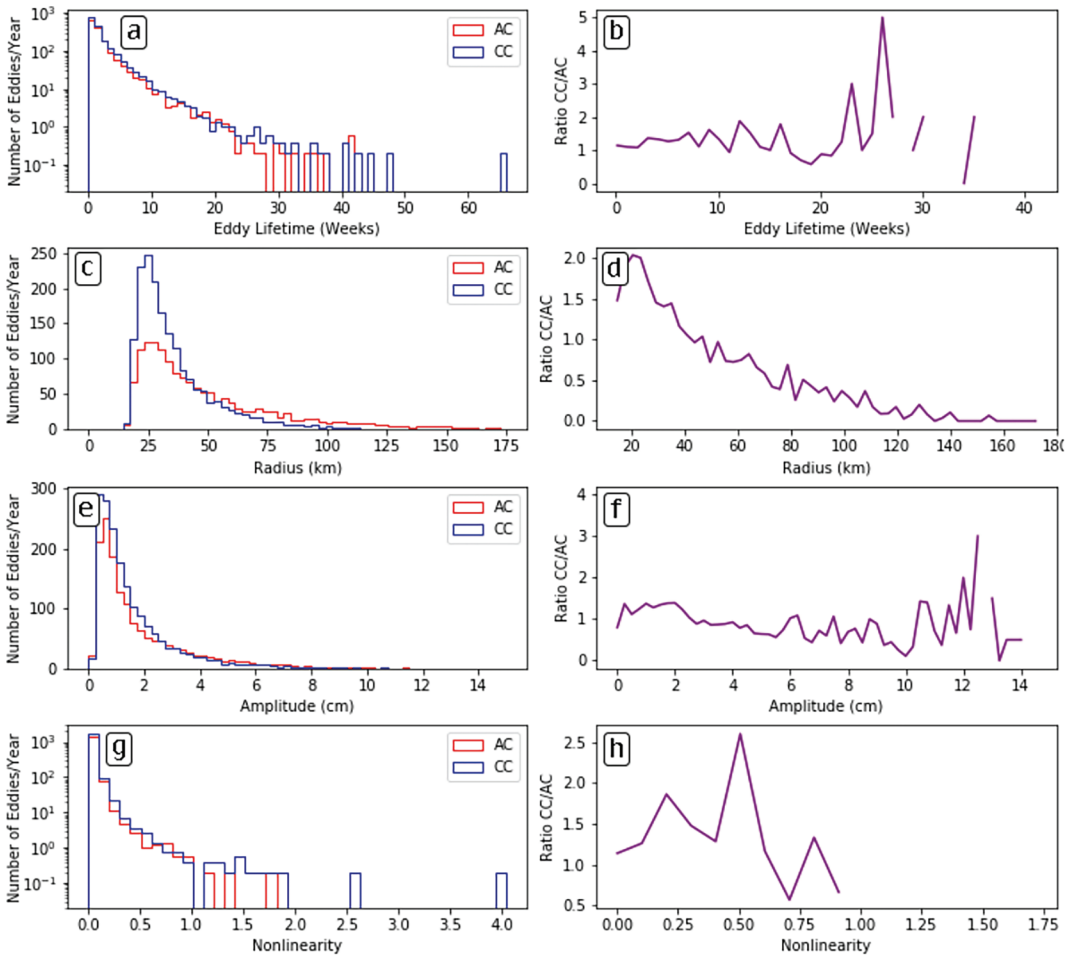

Figure 7. Statistical comparisons for cyclones (blue) and anticyclones (red). Plots show (a and b) eddy lifetime, (c and d) radius, (e and f) amplitude, and (g and h) nonlinearity against number of eddies per year and ratio of CC/AC. CC = cyclonic eddies; AC = anticyclonic eddies.

eddies and the previously discussed higher cyclonic activity (Figures 6f and 6g) support the recently observed correlations between eddy intensities, swirl speeds, and nonlinearities (Gaube et al., 2015). Inspections of a decadal record of NASA's satellite scatterometer (QuikSCAT) suggest that the trade winds tend to be strong and persistent during summer and variable during winter (Jia et al., 2011). Trade wind conditions leeward of the Main Hawai'ian Islands are characterized by positive (negative) wind stress curl in the northern (southern) leeward region, consistent with earlier observations of Smith and Grubišić (1993). Using NOGAPS and ASCAT products, we could not judge if the area of positive wind stress curl was larger than the area of negative wind stress curl. The reason for higher frequency of cyclonic eddy births is unclear at present, and it will form a good topic for future research.

3.4. Influence of Nonlinearities on Larval Fish Dispersal

Both submesoscale and mesoscale eddies play an important role in the dynamics of the world's oceans, mediating both the horizontal and vertical transport of physical, chemical, and biological tracers (e.g., Forget et al., 2015; Gaube et al., 2013; Lindo-Atichati et al., 2012, 2016; Mullaney & Suthers, 2013). Ocean eddy fluxes become critical for problems ranging from climate change to CO_2 air-sea exchanges, and from ocean primary production to larval dispersal (Beal et al., 2011; Chelton et al., 2011; Moreau et al., 2017; Wren et al., 2016). The comprehensive analysis of eddy activity and properties in the Hawai'ian Archipelago presented in this work will enable us to explore the linkages between eddy activity and coral reef fish by (1) comparing the spatial distribution of simulated eddies with distinct characteristics and the observed spawning locations of coral reef fish and (2) comparing the temporal evolution of simulated eddies and the observed spawning sea son of reef fish. Here larval retention refers to the process by which larvae end their pelagic larval duration

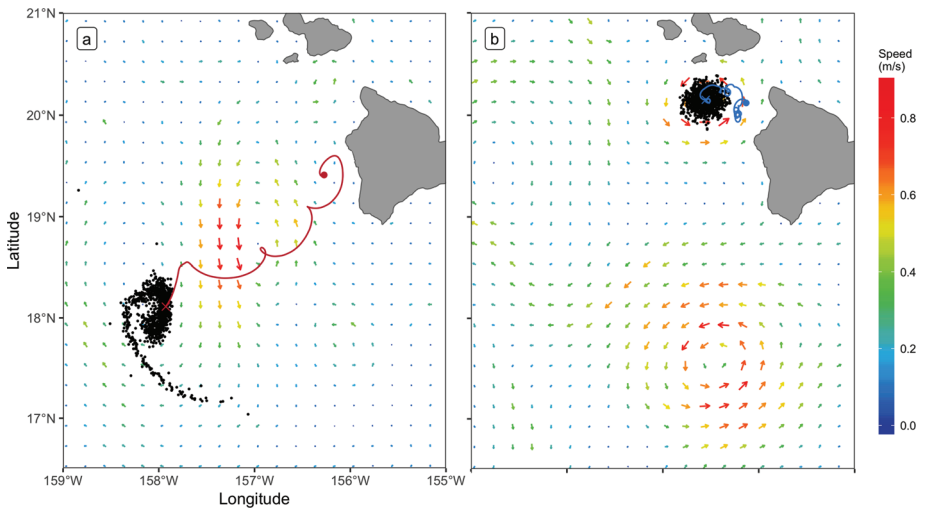

Figure 8. Distribution of synthetic coral reef larval fish at the end of their pelagic larval duration when they are released in eddies with different nonlinearities. (a) Start location of 1,000 larval fish at the center of a linear anticyclonic eddy on 25 November 2011 (red dot), average trajectory of all larval fish during their pelagic larval duration (red curve), individual end locations (black dots), and average end location (red cross) of all larval fish on 8 January 2012. (b) Start location of 1,000 larval fish at the center of a nonlinear cyclonic eddy on 20 April 2010 (blue dot), average trajectory of all larval fish during a pelagic larval duration of 45 days (blue curve), and individual end locations (black dots) and average end location (blue cross) of larval fish on 3 June 2010. Surface geostrophic currents from MITgcm are superimposed for the end day of each simulation. The current velocity fields range from 0.1 to 1 m s^{-1}. The Rossby wave speed in Hawai'i from 15° N to 30° N ranges from 0.05 to 0.15 m s^{-1} (Van Woert & Price, 1993). The lifetime of both eddies is longer than the duration of the simulations.

in proximity to potential insular fish habitat. Although that proximity distance is a subjective term and region dependent, we defined proximity as intermediate scales less than 40 km. Literature usually uses spatial scales greater than 100 km for processes affecting between-islands dispersal to operate (Largier, 2003; Shanks et al., 2003; Swearer et al., 1999).

Spatially, reef fish spawning locations are likely throughout the islands' coastal areas based on adult patterns of abundance reported by McCoy et al. (2017). As presented in section 3.1, some of these locations, especially windward and leeward of the Main Hawai'ian Islands, are also regions of high eddy activity. Average eddy activity (of both polarities) near reef spawning locations windward and leeward of the Main Hawai'ian Islands is close to 40 eddies per year with local peaks of eddy activity closer to 80 eddies per year (Figures 2b and 2c).

Temporally, reef fish spawning season in the Hawai'ian Archipelago does not appear to be related with the timing of eddy births windward and leeward of the main Hawai'ian Islands. A comprehensive survey of reef fish spawning and recruitment in West Hawai'i found that recruitment peaked in June–July with a secondary peak in February–March; however, there was a significant interannual variability for many species that remained unexplained yet was likely related to physical advective/retentive processes (Walsh, 1987). Interestingly, reef fish spawning season in the whole Hawai'ian Archipelago coincides with the spring season of high eddy activity for the whole of the analysis region of the North Pacific presented here using a modeling framework.

Eddies with distinct nonlinearity characteristics lead to different patterns of larval retention of reef fish. We observed that nonlinear eddies kept larval fish entrained and concentrated to a greater extent than linear eddies. For example, a linear mesoscale anticyclonic eddy originated 37 km west of the Big Island in proximity to potential insular fish habitat on 25 November 2011 (Figure 8a, red dot). The average amplitude, radius, intensity, lifetime, and nonlinearity of that eddy were 1 cm, 25 km, 0.03 cm/km, 110 days, and 0.03. A total of 1,000 synthetic larval fish were released at the surface of the eddy centroid and tracked during a 45-day period, which is a typical pelagic larval duration for coral reef larval fish. Synthetic larvae dispersed southwest away from the Main Hawai'ian Islands in a corkscrew-resembling average path and covered a linear distance of 226 km from the release site to the average end location of all larvae (Figure 8a, red cross). They were dispersed a mean distance (mean ± SD) of 239 ± 54 km away from the nearest reef habitat and 95%

of larval fish spread a maximum distance of 291 km at the end of the 45-day dispersal period. Conversely, a nonlinear mesoscale cyclonic eddy originated 25 km west of the Big Island in proximity to potential insular fish habitat on 20 April 2010 (Figure 8b, blue dot). The average amplitude, radius, intensity, lifetime, and nonlinearity of that eddy were 12 cm, 38 km, 0.3 cm/km, 133 days, and 2.11. Similarly, 1,000 synthetic larval fish were released at the centroid of the eddy and tracked during a 45-day period. Synthetic larvae remained entrained by the nonlinear eddy and relatively stationary, covering only a linear distance of 44 km from the release site to the average end location of all larvae (Figure 8b, blue cross). They were dispersed a mean distance (mean ± SD) of 37 ± 9 km away from the nearest reef habitat and 95% of larval fish spread a maximum distance of 35 km at the end of the 45-day dispersal period. Notably, none of these two eddies were embedded in a main current system. The linear anticyclonic eddy (Figure 8a) was located away from any main current system in between the HLC, HLCC, and NEC. The nonlinear anticyclonic eddy (Figure 8b) was located away from any main current system south of the HLC. These findings are very important to better understand the biological imprint that eddies transport: Nonlinear eddies have been observed to trap inside them higher levels of chlorophyll compared to linear eddies (Liu et al., 2013), and nonlinear eddies have been hypothesized to trap more planktonic communities than linear eddies (McGillicuddy Jr, 2016). Here we confirm that westward propagating nonlinear eddies that are not embedded in main current systems favor larval retenti on of reef fish in oceanic islands, while westward propagating linear eddies favor dispersion of reef fish in oceanic islands. Additional simulations of larval dispersion in eddies of different nonlinearities and polarities are provided in Texts S1–S3 and Figures S1–S3 in the supporting information.

4. Conclusion and Prospect

This study presents a quantitative analysis of eddy characteristics in the Hawai‘ian Archipelago, including temporal variability of eddy generation, spatial distribution of eddy properties (births, pathways, amplitudes, radii, intensities, and lifetimes), and ratio of cyclonic and anticyclonic polarities in some of the properties as well as nonlinearity.

To conduct this Eulerian assessment of eddy activity, we took advantage of 5 years of sea level anomalies from a MITgcm simulation for the Hawai‘ian Archipelago. The modeled eddy activity of course could be refined further. For example, it only provides a crude estimate of eddy activity and properties in a statistical sense. We suspect that using a credible reanalysis product of high resolution as an input for the eddy identification and tracking would enhance the accuracy of the estimates. Also, there is a certain degree of skewness associated with the assumption of geostrophic balance, used in deriving surface velocities from sea level anomalies. The difference in Rossby number between that computed from the model's surface velocity and that from the model's surface geostrophic velocity shows that anticyclonic eddy rotation is mostly underestimated by the geostrophic flow and cyclonic eddy rotation is mostly overestimated by the geostrophic flow, especially for eddies in the vicinity of the Big Island of Hawai‘i (Figures S6 and S7). The absence of cyclostrophic effects is likely a dominant source of error. Since the swirl (rotational) speeds of eddies from the eddy tracking algorithm were evaluated based on geostrophic balance, a direct consequence of under (over) estimation of eddy rotation was to skew anticyclonic (cyclonic) eddies toward being identified as linear (nonlinear). This may partially explain the dominance of nonlinear cyclonic eddies over anticyclonic ones. In addition, the geostrophic approximation may also lead to more cyclonic eddies being detected than anticyclonic ones, higher intensity and longer lifetime of cyclonic eddies than anticyclonic ones. We believe that this skewness also exists when eddy tracking in the world oceans is carried out using SLA derived from altimetric observations. A possible remedy would be to include cyclostrophic effects in the evaluation of the swirl speed in the eddy tracking algorithm.

We found that cyclonic (anticyclonic) eddy genesis was prevalent nearshore (offshore) over the NHRC. Eddy genesis of both polarities was prevalent over the islands' leeward region. The latter pattern resembled closely the dipole structures in the curl of the wind stress in the region. Our results support the wind forcing mechanism for eddy formation in the immediate west of the islands; the regions of cyclonic (anticyclonic) eddy birth coincide with the positive (negative) poles in the wind stress curl. Temporally, cyclonic (anticyclonic)

eddy genesis was 30% (35%) higher in spring than in fall. Our analysis provides the first confirmation of that seasonality for the whole study region. Eddy births, intensities, and radii were significantly lower for anticyclones than for cyclones. The distribution of eddy lifetimes, the distribution of radii, and distribution of amplitudes versus the annual number of eddies were lognormal. Remarkably, the number of eddies with lifetimes between 1 and 5 weeks, radii between 30 and 60 km, and amplitudes between 1 and 5 cm decreased tenfold. There were more nonlinear cyclones than anticyclones in the region, which explains the higher regional cyclonic eddy activity.

The focus of this study is on the Eulerian assessment of eddy properties in the Hawai'ian archipelago. It adds to and reconciles with the rich diversity of studies on eddy activities in the region. We have also provided a few examples of Lagrangian larval dispersal to demonstrate the complex seascape that marine species subsist within and the variety of dispersal patterns that emerged from eddies of different properties. For the period and region of our study, nonlinear eddies that are not embedded within a main current system have a higher likelihood to retain larvae near their spawning sites than linear eddies or nonlinear eddies that are embedded within a main current system. This is our first step toward a fully global characterization of physical-biological interactions in an eddy environment with the goal to determine what regime of eddy activities are beneficial for larval fish retention and connectivity among oceanic islands.

Acknowledgments
This work was supported by the National Ocean and Atmospheric Administration (NOAA) Fisheries And The Environment (FATE) Award WE133F17SE1020. This work used the Extreme Science and Engineering Discovery Environment (XSEDE), which is supported by the National Science Foundation Grant NSF-OCE170005. Data supporting the analysis and conclusions are publicly available (at http://doi.org/10.5281/zenodo.3722555). We thank C. Valencia, M. Ho, J. Oquist, and M. Desai for their assistance with data visualization. Earlier drafts benefited from comments of K. Shulzitski.

References

Abernathey, R., & Haller, G. (2018). Transport by Lagrangian vortices in the eastern Pacific. *Journal of Physical Oceanography*, *48*(3), 667–685.

Amante, C., & Eakins, B. W. (2009). ETOPO1 arc-minute global relief model: Procedures, data sources and analysis. http://www.ngdc.noaa.gov/mgg/global/global.html

Amores, A., Melnichenko, O., & Maximenko, N. (2017). Coherent mesoscale eddies in the North Atlantic Subtropical Gyre: 3-D structure and transport with application to the salinity maximum. *Journal of Geophysical Research: Oceans*, *122*, 23–41. ttps://doi.org/10.1002/2016JC012256

Ashkezari, M. D., Hill, C. N., Follett, C. N., Forget, G., & Follows, M. J. (2016). Oceanic eddy detection and lifetime forecast using machine learning methods. *Geophysical Research Letters*, *43*, 12,234–12,241. https://doi.org/10.1002/2016GL071269

Beal, L. M., De Ruijter, W. P., Biastoch, A., Zahn, R., Cronin, M., Hermes, J., et al. (2011). On the role of the Agulhas system in ocean circulation and climate. *Nature*, *472*(7344), 429.

Bentamy, A., & Croize-Fillon, D. (2012). Gridded surface wind fields from METOP/ASCAT measurements. *International Journal of Remote Sensing*, *33*(6), 1729–1754.

Calil, P. H., Richards, K. J., Jia, Y., & Bidigare, R. R. (2008). Eddy activity in the lee of the Hawaiian islands. *Deep Sea Research Part II: Topical Studies in Oceanography*, *55*(10-13), 1179–1194.

Castillo-Trujillo, A. C., Partridge, D., Powell, B., & Flament, P. (2019). Vorticity balance off the south shore of Oahu, Hawaii, derived by high-frequency radio Doppler current observations. *Journal of Physical Oceanography*, *49*(1), 211–225.

Chaigneau, A., Le Texier, M., Eldin, G., Grados, C., & Pizarro, O. (2011). Vertical structure of mesoscale eddies in the eastern south Pacific Ocean: A composite analysis from altimetry and argo profiling floats. *Journal of Geophysical Research*, *116*, C11025. https://doi.org/10.1029/2011JC007134

Chassignet, E. P., Hurlburt, H. E., Metzger, E. J., Smedstad, O. M., Cummings, J. A., Halliwell, G. R., Bleck, R., Baraille, R., Wallcraft, A. J., Lozano, C., Tolman, H. L., Srinivasan, A., Hankin, S., Cornillon, P., Weisberg, R., Barth A., He, R., Werner, F., & Wilkin, J. (2009). US GODAE: global ocean prediction with the HYbrid Coordinate Ocean Model (HYCOM). *Oceanography*, *22*(2), 64–75.

Chavanne, C., Flament, P., & Gurgel, K.-W. (2010). Interactions between a submesoscale anticyclonic vortex and a front. *Journal of Physical Oceanography*, *40*(8), 1802–1818.

Chavanne, C., Flament, P., Lumpkin, R., Dousset, B., & Bentamy, A. (2002). Scatterometer observations of wind variations induced by oceanic islands: Implications for wind-driven ocean circulation. *Canadian Journal of Remote Sensing*, *28*(3), 466–474.

Chavanne, C., & Klein, P. (2010). Can oceanic submesoscale processes be observed with satellite altimetry? *Geophysical Research Letters*, *37*, L22602. https://doi.org/10.1029/2010GL045057

Chelton, D. B., Deszoeke, R. A., Schlax, M. G., El Naggar, K., & Siwertz, N. (1998). Geographical variability of the first baroclinic Rossby radius of deformation. *Journal of Physical Oceanography*, *28*(3), 433–460.

Chelton, D. B., Gaube, P., Schlax, M. G., Early, J. J., & Samelson, R. M. (2011). The influence of nonlinear mesoscale eddies on near-surface oceanic chlorophyll. *Science*, *334*(6054), 328–332.

Chelton, D. B., Schlax, M. G., & Samelson, R. M. (2011). Global observations of nonlinear mesoscale eddies. *Progress in Oceanography*, *91*(2), 167–216.

Chelton, D. B., Schlax, M. G., Samelson, R. M., & de Szoeke, R. A. (2007). Global observations of large oceanic eddies. *Geophysical Research Letters*, *34*, L15606. https://doi.org/10.1029/2007GL030812

Chen, S., & Qiu, B. (2010). Mesoscale eddies northeast of the Hawaiian Archipelago from satellite altimeter observations. *Journal of Geophysical Research*, *115*, C03016. https://doi.org/10.1029/2009JC005698

Cheng, Y.-H., Ho, C.-R., Zheng, Q., & Kuo, N.-J. (2014). Statistical characteristics of mesoscale eddies in the North Pacific derived from satellite altimetry. *Remote Sensing*, *6*(6), 5164–5183.

Dee, D. P., Uppala, S. M., Simmons, A., Berrisford, P., Poli, P., Kobayashi, S., et al. (2011). The ERA-Interim reanalysis: Configuration and performance of the data assimilation system. *Quarterly Journal of the Royal Meteorological Society*, *137*(656), 553–597.

Dickey, T. D., Nencioli, F., Kuwahara, V. S., Leonard, C., Black, W., Rii, Y. M., et al. (2008). Physical and bio-optical observations of oceanic cyclones west of the island of Hawai'i. *Deep Sea Research Part II: Topical Studies in Oceanography*, *55*(10-13), 1195–1217.

Dong, C., Mavor, T., Nencioli, F., Jiang, S., Uchiyama, Y., McWilliams, J. C., et al. (2009). An oceanic cyclonic eddy on the lee side of Lanai Island, Hawai'i. *Journal of Geophysical Research*, *114*, C10008. \ignorespaceshttps://doi.org/10.1029/2009JC005346

Faghmous, J. H., Frenger, I., Yao, Y., Warmka, R., Lindell, A., & Kumar, V. (2015). A daily global mesoscale ocean eddy dataset from satellite altimetry. *Scientific Data*, *2*, 150,028.

Forget, G., Ferreira, D., & Liang, X. (2015). On the observability of turbulent transport rates by argo: Supporting evidence from an inversion experiment. *Ocean Science*, *11*(5), 839.

Frenger, I., Münnich, M., Gruber, N., & Knutti, R. (2015). Southern ocean eddy phenomenology. *Journal of Geophysical Research: Oceans*, *120*, 7413–7449. https://doi.org/10.1002/2015JC011047

Gaube, P., Chelton, D. B., Samelson, R. M., Schlax, M. G., & O'Neill, L. W. (2015). Satellite observations of mesoscale eddy-induced Ekman pumping. *Journal of Physical Oceanography*, *45*(1), 104–132.

Gaube, P., Chelton, D. B., Strutton, P. G., & Behrenfeld, M. J. (2013). Satellite observations of chlorophyll, phytoplankton biomass, and Ekman pumping in nonlinear mesoscale eddies. *Journal of Geophysical Research: Oceans*, *118*, 6349–6370. https://doi.org/10.1002/2013JC009027

Griffa, A. (1996). Applications of stochastic particle models to oceanographic problems, *Stochastic modelling in physical oceanography* (pp. 113–140). Springer.

Haller, G. (2015). Lagrangian coherent structures. *Annual Review of Fluid Mechanics*, *47*, 137–162.

Hausmann, U., & Czaja, A. (2012). The observed signature of mesoscale eddies in sea surface temperature and the associated heat transport. *Deep Sea Research Part I: Oceanographic Research Papers*, *70*, 60–72.

Howell, E. A., Bograd, S. J., Morishige, C., Seki, M. P., & Polovina, J. J. (2012). On North Pacific circulation and associated marine debris concentration. *Marine Pollution Bulletin*, *65*(1-3), 16–22.

Isern-Fontanet, J., García-Ladona, E., & Font, J. (2003). Identification of marine eddies from altimetric maps. *Journal of Atmospheric and Oceanic Technology*, *20*(5), 772–778.

Jia, Y., Calil, P., Chassignet, E., Metzger, E., Potemra, J., Richards, K., & Wallcraft, A. J. (2011). Generation of mesoscale eddies in the lee of the Hawaiian islands. *Journal of Geophysical Research*, *116*, C11009. https://doi.org/10.1029/2011JC007305

Kersale, M., Doglioli, A., & Petrenko, A. (2011). Sensitivity study of the generation of mesoscale eddies in a numerical model of Hawaii islands. *Ocean Science*, *7*(3), 277–291.

Kobashi, F., & Kawamura, H. (2002). Seasonal variation and instability nature of the North Pacific subtropical countercurrent and the Hawaiian lee countercurrent. *Journal of Geophysical Research*, *107*(C11), 6–1.

Kurian, J., Colas, F., Capet, X., McWilliams, J. C., & Chelton, D. B. (2011). Eddy properties in the California Current System. *Journal of Geophysical Research*, *116*, C08027. https://doi.org/10.1029/2010JC006895

LaCasce, J. (2008). Statistics from lagrangian observations. *Progress in Oceanography*, *77*(1), 1–29.

Lange, M., & van Sebille, E. (2017). Parcels v0. 9: prototyping a Lagrangian ocean analysis framework for the petascale age. arXiv preprint arXiv:1707.05163.

Large, W. G., McWilliams, J. C., & Doney, S. C. (1994). Oceanic vertical mixing: A review and a model with a nonlocal boundary layer parameterization. *Reviews of Geophysics*, *32*(4), 363–403.

Large, W., & Pond, S. (1981). Open ocean momentum flux measurements in moderate to strong winds. *Journal of Physical Oceanography*, *11*(3), 324–336.

Large, W., & Pond, S. (1982). Sensible and latent heat flux measurements over the ocean. *Journal of Physical Oceanography*, *12*(5), 464–482.

Largier, J. L. (2003). Considerations in estimating larval dispersal distances from oceanographic data. *Ecological Applications*, *13*(sp1), 71–89.

Lindo-Atichati, D., Bringas, F., Goni, G., Muhling, B., Muller-Karger, F. E., & Habtes, S. (2012). Varying mesoscale structures influence larval fish distribution in the Northern Gulf of Mexico. *Marine Ecology Progress Series*, *463*, 245–257.

Lindo-Atichati, D., Curcic, M., Paris, C. B., & Buston, P. M. (2016). Description of surface transport in the region of the Belizean barrier reef based on observations and alternative high-resolution models. *Ocean Modelling*, *106*, 74–89.

Lindo-Atichati, D., Montero, P., Rodil, R., Quintana, J. B., & Miró, M. (2019). Modeling dispersal of UV filters in estuaries. *Environmental Science & Technology*, *53*(3), 1353–1363.

Lindo-Atichati, D., Paris, C., Le HÉnaff M., Schedler, M., Juárez, A. V., & Müller, R. (2016). Simulating the effects of droplet size, high-pressure biodegradation, and variable flow rate on the subsea evolution of deep plumes from the Macondo blowout. *Deep Sea Research Part II: Topical Studies in Oceanography*, *129*, 301–310.

Liu, Y., Dong, C., Guan, Y., Chen, D., McWilliams, J., & Nencioli, F. (2012). Eddy analysis in the subtropical zonal band of the North Pacific Ocean. *Deep Sea Research Part I: Oceanographic Research Papers*, *68*, 54–67.

Liu, F., Tang, S., & Chen, C. (2013). Impact of nonlinear mesoscale eddy on phytoplankton distribution in the northern South China Sea. *Journal of Marine Systems*, *123*, 33–40.

Lumpkin, C. F. (1998). Eddies and currents of the Hawaiian islands (PhD Thesis), University of Hawaii at Manoa.

Lynch, D. R., Greenberg, D. A., Bilgili, A., McGillicuddy Jr, D. J., Manning, J. P., & Aretxabaleta, A. L. (2014). *Particles in the coastal ocean: Theory and applications*. Cambridge: Cambridge University Press.

Mariano, A. J., Griffa, A., Özgökmen, T. M., & Zambianchi, E. (2002). Lagrangian analysis and predictability of coastal and ocean dynamics 2000. *Journal of Atmospheric and Oceanic Technology*, *19*(7), 1114–1126.

Marshall, J., Adcroft, A., Hill, C., Perelman, L., & Heisey, C. (1997). A finite-volume, incompressible Navier stokes model for studies of the ocean on parallel computers. *Journal of Geophysical Research*, *102*(C3), 5753–5766.

Mason, E., Pascual, A., Gaube, P., Ruiz, S., Pelegrí, J. L., & Delepoulle, A. (2017). Subregional characterization of mesoscale eddies across the Brazil-Malvinas Confluence. *Journal of Geophysical Research: Oceans*, *122*, 3329–3357. https://doi.org/10.1002/2016JC012611

Mason, E., Pascual, A., & McWilliams, J. C. (2014). A new sea surface height–based code for oceanic mesoscale eddy tracking. *Journal of Atmospheric and Oceanic Technology*, *31*(5), 1181–1188.

Maximenko, N. A., Bang, B., & Sasaki, H. (2005). Observational evidence of alternating zonal jets in the world ocean. *Geophysical Research Letters*, *32*, L12607. https://doi.org/10.1029/2005GL022728

Maximenko, N. A., Melnichenko, O. V., Niiler, P. P., & Sasaki, H. (2008). Stationary mesoscale jet-like features in the ocean. *Geophysical Research Letters*, *35*, L08603. https://doi.org/10.1029/2008GL033267

McCoy, K., Heenan, A., Asher, J., Ayotte, P., Gorospe, K., Gray, A., et al. (2017). Pacific reef assessment and monitoring program data report, ecological monitoring 2016—Reef fishes and benthic habitats of the main Hawaiian islands, northwestern Hawaiian islands, Pacific remote island areas, and American Samoa. Pacific Islands Fisheries Science Center Data Report, DR-17-001.

McGillicuddy Jr, D. J. (2016). Mechanisms of physical-biological-biogeochemical interaction at the oceanic mesoscale.

Melnichenko, O., Amores, A., Maximenko, N., Hacker, P., & Potemra, J. (2017). Signature of mesoscale eddies in satellite sea surface salinity data. *Journal of Geophysical Research: Oceans*, *122*, 1416–1424. https://doi.org/10.1002/2016JC012420

Moreau, S., Penna, A. D., Llort, J., Patel, R., Langlais, C., Boyd, P. W., et al. (2017). Eddy-induced carbon transport across the antarctic circumpolar current. *Global Biogeochemical Cycles*, *31*, 1368–1386.

Mullaney, T. J., & Suthers, I. M. (2013). Entrainment and retention of the coastal larval fish assemblage by a short-lived, submesoscale, frontal eddy of the East Australian Current. *Limnology and Oceanography*, *58*(5), 1546–1556.

Mysak, L. A., & Magaard, L. (1983). Rossby wave driven Eulerian mean flows along non-zonal barriers, with application to the Hawaiian ridge. *Journal of Physical Oceanography*, *13*(9), 1716–1725.

Nakano, H., & Hasumi, H. (2005). A series of zonal jets embedded in the broad zonal flows in the Pacific obtained in eddy-permitting ocean general circulation models. *Journal of Physical Oceanography*, *35*(4), 474–488.

Okubo, A. (1970). Horizontal dispersion of floatable particles in the vicinity of velocity singularities such as convergences. In *Deep sea research and oceanographic abstracts*, *17*, Elsevier, pp. 445–454.

Patzert, W. C. (1969). Eddies in Hawaiian waters: HAWAII INST OF GEOPHYSICS HONOLULU.

Peacock, T., Froyland, G., & Haller, G. (2015). *Introduction to focus issue: Objective detection of coherent structures*: AIP Publishing.

Pegliasco, C., Chaigneau, A., & Morrow, R. (2015). Main eddy vertical structures observed in the four major eastern boundary upwelling systems. *Journal of Geophysical Research: Oceans*, *120*, 6008–6033.

Penven, P., Echevin, V., Pasapera, J., Colas, F., & Tam, J. (2005). Average circulation, seasonal cycle, and mesoscale dynamics of the Peru current system: A modeling approach. *Journal of Geophysical Research*, *110*, C10021. https://doi.org/10.1029/2005JC002945

Powell, B. (2017). Quantifying how observations inform a numerical reanalysis of Hawaii. *Journal of Geophysical Research: Oceans*, *122*, 8427–8444. https://doi.org/10.1002/2017JC012854

Price, J. M., Van Woert, M. L., & Vitousek, M. (1994). On the possibility of a ridge current along the Hawaiian islands. *Journal of Geophysical Research*, *99*(C7), 14,101–14,111.

Qiu, B., & Chen, S. (2010). Interannual variability of the North Pacific subtropical countercurrent and its associated mesoscale eddy field. *Journal of Physical Oceanography*, *40*(1), 213–225.

Qiu, B., Koh, D. A., Lumpkin, C., & Flament, P. (1997). Existence and formation mechanism of the North Hawaiian Ridge Current. *Journal of Physical Oceanography*, *27*(3), 431–444.

Rhines, P. B. (1975). Waves and turbulence on a beta-plane. *Journal of Fluid Mechanics*, *69*(3), 417–443.

Richards, K. J., Maximenko, N. A., Bryan, F. O., & Sasaki, H. (2006). Zonal jets in the Pacific Ocean. *Geophysical Research Letters*, *33*, L03605. https://doi.org/10.1029/2005GL024645

Schütte, F., Brandt, P., & Karstensen, J. (2016). Occurrence and characteristics of mesoscale eddies in the tropical northeast Atlantic Ocean. *Ocean Science*, *12*(3), 663–685.

Shakespeare, C. J. (2016). Curved density fronts: Cyclogeostrophic adjustment and frontogenesis. *Journal of Physical Oceanography*, *46*(10), 3193–3207.

Shanks, A. L., Grantham, B. A., & Carr, M. H. (2003). Propagule dispersal distance and the size and spacing of marine reserves. *Ecological Applications*, *13*(sp1), 159–169.

Smith, R. B., & Grubišić, V. (1993). Aerial observations of Hawaii's wake. *Journal of the Atmospheric Sciences*, *50*(22), 3728–3750.

Soufflet, Y., Marchesiello, P., Lemarié, F., Jouanno, J., Capet, X., Debreu, L., & Benshila, R. (2016). On effective resolution in ocean models. *Ocean Modelling*, *98*, 36–50.

Swearer, S. E., Caselle, J. E., Lea, D. W., & Warner, R. R. (1999). Larval retention and recruitment in an island population of a coral-reef fish. *Nature*, *402*(6763), 799.

Van Sebille, E., Griffies, S. M., Abernathey, R., Adams, T. P., Berloff, P., Biastoch, A., et al. (2017). Lagrangian ocean analysis: Fundamentals and practices. *Ocean Modelling*.

Van Woert, M. L., & Price, J. M. (1993). Geosat and advanced very high resolution radiometer observations of oceanic planetary waves adjacent to the hawaiian islands. *Journal of Geophysical Research*, *98*(C8), 14,619–14,631.

Walsh, W. (1987). Patterns of recruitment and spawning in Hawaiian reef fishes. *Environmental Biology of Fishes*, *18*(4), 257–276.

Wang, Z., Li, Q., Sun, L., Li, S., Yang, Y., & Liu, S. (2015). The most typical shape of oceanic mesoscale eddies from global satellite sea level observations. *Frontiers of Earth Science*, *9*(2), 202–208.

Weiss, J. (1991). The dynamics of enstrophy transfer in two-dimensional hydrodynamics. *Physica D: Nonlinear Phenomena*, *48*(2-3), 273–294.

White, W. (1983). A narrow boundary current along the eastern side of the Hawaiian Ridge; the North Hawaiian Ridge Current. *Journal of Physical Oceanography*, *13*(9), 1726–1731.

Wren, J. L., Kobayashi, D. R., Jia, Y., & Toonen, R. J. (2016). Modeled population connectivity across the Hawaiian Archipelago. *PloS One*, *11*(12), e0167626.

Xie, S.-P., Liu, W. T., Liu, Q., & Nonaka, M. (2001). Far-reaching effects of the Hawaiian islands on the Pacific Ocean-Atmosphere System. *Science*, *292*(5524), 2057–2060.

Yu, Z., Maximenko, N., Xie, S.-P., & Nonaka, M. (2003). On the termination of the Hawaiian Lee Countercurrent. *Geophysical Research Letters*, *30*(5), 1215. https://doi.org/10.1029/2002GL016710

Zhang, Y., Kieft, B., Hobson, B. W., Ryan, J. P., Barone, B., Preston, C. M., et al. (2019). Autonomous tracking and sampling of the deep chlorophyll maximum layer in an open-ocean eddy by a long-range autonomous underwater vehicle. *IEEE Journal of Oceanic Engineering*, 1–19.